

# **POLARIMETRIC MICROWAVE BRIGHTNESS SIGNATURES OF OCEAN WIND DIRECTIONS**

Simon H. Yueh, William J. Wilson, Steven J. Dinardo, and Fuk K. Li

Jet Propulsion Laboratory  
California Institute of Technology  
4800 Oak Grove Drive  
Pasadena, CA 91109  
Tel: (818) 354-3012, Fax: (818) 393-3077

Submitted to IEEE Trans. Geosci. Remote Sensing in December 1997

## Abstract

The sensitivities of wind direction signals in passive microwave brightness temperatures of sea surfaces to wind speed, incidence angle, polarization, and frequency are presented in this paper. The experimental data were acquired from a series of aircraft flights from 1994 through 1996 by the Jet Propulsion Laboratory (JPL) using JPL 19 and 37 GHz polarimetric radiometers (WINDRAD). Fourier analysis of the data versus wind direction was carried out and the coefficients of Fourier series are illustrated against the wind speed at  $45^\circ$ ,  $55^\circ$ , and  $65^\circ$  incidence angles. There is a good agreement between the JPL aircraft flight data and Wentz's SSM/I geophysical model function for the vertically polarized brightness temperatures, but Wentz's SSM/I wind direction model for horizontal polarization shows a significantly stronger upwind and downwind asymmetry than the aircraft flight data. Comparison of the dual-frequency WINDRAD data shows that the wind direction signals are similar at 19 and 37 GHz, although the 37 GHz data have slightly stronger signals than the 19 GHz data. In general, the azimuthal variations of brightness temperatures increase with increasing wind speed from low to moderate winds, then level off and decrease at high winds. The only exception is the  $U$  measurements at  $65^\circ$  incidence angle, which have a stronger than expected signal at low winds. An exponential function was proposed to model the sensitivities of wind direction signals to wind speeds. The coefficients of the empirical model are provided in this paper and are useful for the simulation of ocean brightness temperatures and for the development of geophysical retrieval algorithms.

# 1 Introduction

There has been an increasing interest in the passive polarimetric microwave signatures of the ocean surface wind velocity (speed and direction) [1, 2, 3, 4, 5, 6, 7, 8]. The sensitivity of sea surface brightness temperatures to ocean wind speed has been demonstrated in many early studies and has been applied to global measurements of ocean surface wind speed using spaceborne radiometers, such as the Scanning Multichannel Microwave Radiometer (SMMR) flown on NIMBUS-7 and SEASAT and the Special Sensor Microwave/Imager (SSM/I) deployed on the Defense Meteorological Satellite Program (DMSP) missions [2].

However, recent experimental and theoretical studies have shown that there are wind direction signals in sea surface brightness temperatures. The airborne radiometer experiments performed by Russian scientists at the Space Research Institute (SRI) indicated that the vertically and horizontally polarized microwave radiation from sea surfaces vary with the wind direction at near normal incidence angles [3, 4]. The analysis of SSM/I19 and 37 GHz data by Wentz [5] has shown a few Kelvin directional signals in both  $T_v$  and  $T_h$  channels at an incidence angle of  $53^\circ$ . Besides the brightness temperatures of two principal polarizations ( $T_v$  and  $T_h$ ), traditionally used for earth remote sensing, near-nadir looking observations made by Dzura et al. [6] at Ku-band (14 GHz) showed the sensitivity of the third Stokes parameter to wind direction. To explore the polarimetric brightness temperatures of sea surfaces at off-nadir incidence angles, JPL has developed a K-band (19.35 GHz) multi-polarization radiometer (WINDRAD) and deployed it on the National Aeronautics and Space Administration (NASA) DC-8 aircraft with circle flights over several National Data Buoy Center (NDBC) buoys in November 1993 [7]. These measurements demonstrated that the first three Stokes parameters of sea surface emissions are sensitive to ocean wind directions in the incidence angle range of  $30^\circ$  to  $50^\circ$ . Subsequently, JPL added a 37-GHz channel to the WINDRAD and flew the dual-frequency system in 1994 over the NDBC buoys off the California coast to study the frequency sensitivities from  $45^\circ$  to  $65^\circ$  incidence angles [8]. Measured radiometric temperatures showed a few Kelvin azimuth modulations

average of the argument.  $\lambda$  is the electromagnetic wavelength and  $k_B$  is the Boltzmann's constant [1]. The last equality shows that the third and fourth Stokes parameters can be related to the brightness temperatures measured at 45°-linear ( $T_p$ ), -45°-linear ( $T_m$ ), left-hand circular ( $T_l$ ), and right-hand circular ( $T_r$ ) polarizations.

To acquire polarimetric ocean brightness temperatures, a dual-frequency polarimetric radiometer system operating at 19.35 GHz (K band) and 37 GHz (Ka band) was built by the Jet Propulsion Laboratory in 1993 and 1994. A more detailed description of the dual-frequency radiometer system can be found in [7, 8]. The dual-frequency radiometer system was flown on the NASA DC-8 in 1994 and 1995 and on the NASA P-3 in 1996 over the National Data Buoy Center (NDBC) moored buoys, which provided ocean wind speed and direction measurements.

The radiometer antennas were mounted on the aircraft windows at an angle of 75° from nadir. To obtain data at the desired incidence angles of 45°, 55° and 65°, the aircraft was banked at 30°, 20°, and 10°, respectively. At each bank angle, the aircraft performed circle flights around the NDBC buoys, enabling the acquisition of radiometer data from all azimuth angles.

During circle flights, the aircraft pitch and roll drifted in time. The change of pitch angle is typically less than a few tenths of one degree, but will rotate the antenna polarization axes with respect to the radiometer line of sight by about the same amount. A variation of aircraft roll angles, which is typically less than a degree for P-3, but could be as large as a few degrees for DC-8, will result in a change of incidence angles. Since  $U$  is sensitive to the orientation of antenna polarization axes and  $T_v$  and  $T_h$  are sensitive to the change of incidence angles, the changes of aircraft pitch and roll angles need to be corrected. To compensate the variations of aircraft pitch and roll, the aircraft data including time, aircraft heading, roll, pitch and altitude were recorded and were used to calculate the incidence and polarization orientation angles of the antenna. The calculated polarization orientation angle enables the use of a rotation transformation to transform  $T_v$ ,  $T_h$ , and  $U$  measured with respect to the

aircraft coordinate system to the earth surface coordinate. Subsequently, the  $T_v$  and  $T_h$  data were corrected for changes of incidence angles during the circles using measurements from wing-wagging maneuvers in which the aircraft roll angle was slowly varied within about  $\pm 40^\circ$ , which provided the dependence of  $T_v$  and  $T_h$  on incidence angles. More details of the attitude compensation technique are described in [7].

Figure 1 summarizes the total number of circles for aircraft flights from 1994-1996 at each incidence angle for a range of wind speed. Most of low wind ( $< 5 \text{ m}\cdot\text{s}^{-1}$ , circles) and all high wind ( $> 12 \text{ m}\cdot\text{s}^{-1}$ ) cases were acquired when there were clouds over the buoys. Overall, about half of the data were acquired when the skies were clear.

The signatures of the data acquired in 1995 and 1996 do not differ from those of earlier flight data [7, 8]. Figure 2 illustrates the wind direction signals in the first three Stokes parameters at  $55^\circ$  incidence angle under clear sky conditions:  $T_v$ ,  $T_h$ , and  $Q$  have an even symmetry with respect to the wind direction, while  $U$  has an odd symmetry. The signals at 19.35 and 37 GHz are very similar. When there were clouds, the signals in  $T_v$  and  $T_h$  were usually masked out by cloud radiation. The effects of cloud covers are illustrated in Figure 3, which plots the WINDRAD measurements and coincidental ocean backscatter measured by the JPL Ku-band (13.995 GHz) scatterometer (NUSCAT) as a function of antenna azimuth angles. The buoy wind speed was  $15 \text{ m}\cdot\text{s}^{-1}$  at 5 m elevation during flights. There were stratocumulus clouds over the buoy, and the attenuation by atmosphere is about 0.8 dB at 19.35 GHz and about 1.5 dB at 37 GHz at  $55^\circ$  incidence angle. The wind direction signals in  $T_v$ ,  $T_h$ , and  $Q$  are overwhelmed by cloud radiation. However, the signature of  $U$  remains similar to those for clear skies [7, 8] with peaks and dips at about  $45^\circ$  from upwind or downwind directions. The wind direction indicated by the location of zero crossing of  $U$  is consistent with that indicated in radar and buoy measurements. This suggests that  $U$  is nearly insensitive to cloud radiation.

For a few cases when there were sparsely scattered clouds, the difference of  $T_v$  and  $T_h$ , known as  $Q$ , did allow the cancellation of upwelling radiation from clouds and reveal

directional signals of radiation from the surfaces [7]. However, the signals in  $Q$  were often lost for stratus clouds, which consist of many convective cells and are spatially inhomogeneous. This is because the sea surface reflectivity for horizontal polarization increases with increasing incidence angles, but has an opposite trend for vertical polarization. This implies that  $T_h$  is more strongly affected by the downwelling radiation from higher incidence angles, while  $T_v$  is more strongly affected by the downwelling from lower incidence angles. Hence, taking the difference of  $T_v$  and  $T_h$  may not cancel the reflected downwelling cloud radiation from inhomogeneous cloud covers.

### 3 Atmospheric Correction

This section introduces a technique to provide a first order correction of atmospheric effects on the directional signals in sea surface brightness temperatures. The atmosphere influences the sea surface brightness temperatures through atmospheric radiation, attenuation, and scattering. The gases, water vapor, and liquid water in the atmosphere attenuate the microwave radiation from sea surfaces, and the radiation from these atmospheric constituents contributes to the microwave power detected by radiometers. Ignoring the scattering effects by atmosphere, we use a radiative transfer model to account for the effects of atmosphere on the brightness temperatures ( $T_b$ ) measured by radiometers:

$$T_b = \alpha e T_s + T_U + \alpha r T_D \quad (2)$$

where  $\alpha$  amounts for the atmospheric attenuation along the line of sight from the surface to the radiometer,  $e$  is the sea surface emissivity,  $T_s$  is the sea surface temperature (SST),  $T_U$  is the upwelling atmospheric radiation, and  $T_D$  is the downwelling atmospheric radiation.  $r$  is the surface reflectivity. To be exact, the third term should be an integral of downwelling radiation over the upper hemisphere weighted by the bistatic scattering coefficients of the surface. By assuming that the specular reflection dominates the surface reflectivity,  $T_b$  can be approximated by the above equation. Substituting  $r$  by  $1 - e$  based on Kirchhoff's law

[15] results in

$$T_b = AcT_s + B \quad (3)$$

where

$$A = \alpha(1 - \frac{T_D}{T_s}) \quad (4)$$

$$B = T_U + \alpha T_D \quad (5)$$

This model shows that the atmosphere will effectively attenuate the wind velocity signal in the sea surface emissivity,  $e$ , by a factor “A” and adds a hiss “B” to the radiometer observations. Although the microwave radiation from sea surface is only attenuated by one-way loss through the atmosphere, the reflected downwelling sky radiation has a negative impact on the polarized sea surface radiation and effectively introduces an additional attenuation factor:  $1 - T_D/T_s$ .

In the following, we will obtain an approximate relation between A and  $\alpha$ . By ignoring the radiation from cold space,  $T_U$  and  $T_D$  can be approximated by

$$T_U = T_D = T_a(1 - \alpha) \quad (6)$$

where  $T_a$  is the effective air temperature between the surface and water freezing temperatures. Without a significant loss of accuracy,  $T_a$  can be approximated by

$$T_a = (T_s + 273)/2 \quad (7)$$

Using Eqs. (6) and (7), we can rewrite Eq. (4) as:

$$A = \alpha^2 - \alpha(1 - \alpha) \frac{(T_s - 273)}{2T_s} \quad (8)$$

It is straightforward to verify that the second term is in general much smaller than the first term and hence, A can be approximated by:

$$A \approx \alpha^2 \quad (9)$$

This approximation is supported by the relative magnitudes of  $A$  and  $\alpha$  shown in Table 1 evaluated for US standard atmosphere using Liebe's millimeter wave propagation model [20]. The implication is that the effects of atmosphere on the wind direction signals in sea surface brightness temperatures is equivalent to two-way atmospheric attenuation, which is the loss experienced by microwave ocean backscatter.

Substituting Eqs. (4), (5), and (6) into Eq. (3) allows us to obtain an equation for  $\alpha$ . The solution of the equation is:

$$\alpha = \frac{e(T_s - T_a) + \sqrt{e^2(T_s - T_a)^2 + 4T_a(1 - e)(T_a - T_b)}}{2T_a(1 - e)} \quad (10)$$

Because  $T_a$  is usually greater than  $T_b$  and  $T_s$  is greater than  $T_a$ , this solution is positive for most situations.

There are three steps in our approach for the correction of atmospheric effects on wind direction signals in sea surface brightness temperatures. First, the harmonic coefficients defined in Eqs. (12) to (15) were calculated from the aircraft radiometer data. Next,  $A$  and  $\alpha$  are estimated from the  $T_{v0}$  and  $T_{h0}$  acquired at  $55^\circ$ .  $e_v$  and  $e_h$  at  $55^\circ$  incidence angle were estimated from Wentz's SSM/I surface emissivity model [5] using the buoy wind speed and sea surface temperature measurements and were further averaged over wind directions. Eq. (10) then provide an estimate of atmospheric attenuation at  $55^\circ$  incidence angle using  $T_{v0}$  and  $T_{h0}$ . The estimates of  $\alpha$  using  $T_{h0}$  are slightly higher than the estimates using  $T_{v0}$ , but the differences are within 0.1 dB at 19 GHz and within 0.2 dB at 37 GHz. This difference is likely due to various approximations made in leading to the solution of  $\alpha$ . Since the difference is small, an average of these two estimates is taken for data correction. Because circle flights at  $45^\circ$  and  $65^\circ$  incidence angles were carried out before or after the circles at  $55^\circ$  incidence angle for each selected buoy, once  $\alpha$  at  $55^\circ$  incidence angle is estimated,  $\alpha$ 's at the other incidence angles ( $\theta$ ) are approximated by

$$\alpha(\theta) = \frac{\tan \theta}{\tan 55^\circ} \alpha(55^\circ) \quad (11)$$

Note that there were typically two to three consecutive circles at one bank (or incidence)



angle over a selected buoy. Hence,  $\alpha$  estimated using the above technique represents an average of atmospheric losses during those circles. Finally,  $T_{vi}$ ,  $T_{hi}$ ,  $U_i$ , and  $V_i$  for  $i=1$  and  $2$ , were normalized by the effective attenuation  $A$  to estimate these Fourier coefficients for attenuation-free conditions.

Figure 4 illustrates the estimates of  $\alpha(55^\circ)$  at each frequency for the wind speeds and atmospheric conditions encountered. The estimated atmospheric losses vary between 0.3 to 1.5 dB and for most cases are close to 0.35 dB at 19.35 GHz and 0.54 dB at 37 GHz estimated using Liebe's millimeter wave in-coupling model [20] for US standard atmosphere. A large loss factor was observed for the high wind ( $> 15 \text{ m}\cdot\text{s}^{-1}$ ) flights off US east coast on 22 November 1996 when there were thick stratus cloud covers over the buoys. Table 1 also provides an estimate of  $A$  and  $B$  for US standard atmosphere. The effective attenuation ( $A$ ) is 0.85 at 19.35 GHz and 0.77 at 37 GHz. Although the magnitude of  $A$  is not negligible, it is expected that  $A$  can be quite accurately estimated by spaceborne microwave radiometers with multi-frequency channels, except for rains and thick clouds. The more significant effect of atmosphere is the bias term " $B$ ", which is very large compared with the wind direction signals in sea surface radiation. Small variations of atmosphere, for example, thickness changes of cloud layers intercepted by the radiometer antenna beam during a complete  $360^\circ$  aircraft circle, often masked out the direction signals in  $T_v$  and  $T_h$ .

## 4 Fourier Analysis

As shown in the experimental data [7, 8] and an analysis of scattering by reflection symmetric media [14],  $T_v$  and  $T_h$  of the sea surfaces are even functions of  $\phi = \phi_w - \phi_r$  and  $U$  and  $V$  are odd functions of  $\phi$ , where  $\phi_w$  is the direction of wind or wind stress, and  $\phi_r$  is the azimuth angle of radiometer antennas. This enables us to expand the Stokes parameters in cosine or sine series of  $\phi$ . Hence, truncated to the second harmonic of  $\phi$ ,

$$T_v \simeq T_{v0} + T_{v1} \cos \phi + T_{v2} \cos 2\phi \quad (12)$$

$$T_h \simeq T_{h0} + T_{h1} \cos \phi + T_{h2} \cos 2\phi \quad (13)$$

$$U \simeq U_1 \sin \phi + U_2 \sin 2\phi \quad (14)$$

$$V \simeq V_1 \sin \phi + V_2 \sin 2\phi \quad (15)$$

The first harmonics account for the up/downwind asymmetric surface features, while the second harmonics account for the up/crosswind asymmetry. All coefficients are functions of surface wind speed, incidence angle and frequency.

Figures 5 to 13 illustrate the harmonic coefficients (except  $T_{v0}$  and  $T_{h0}$ ) reduced from experimental data as a function of  $U_{N195}$ , the equivalent neutral wind speed at 19.5 m elevation [13]. (The NDBC buoys measure wind speed at 5 m elevation, and the formula by Large and Pond [12] has been used to calculate  $U_{N195}$ .) The data have been corrected for atmospheric attenuation using the method described in the previous section. Because of cloud contamination,  $T_{vi}$ ,  $T_{hi}$ , and  $Q_i$  ( $i=1$  and  $2$ ) obtained under cloudy conditions were excluded. As shown in Figure 1, there was one flight performed at  $45^\circ$  incidence angle near Hurricane Juliette in 1995 with the wind speed near 25 m/s. The signal in  $U$  is similar to that at lower wind speeds. Because there were no circles performed at  $55^\circ$  incidence angle, it was not possible to obtain an estimate of atmospheric attenuation and hence, the data are not plotted.

The general characteristics of 19 and 37 GHz data are very similar in terms of wind speed dependence for each incidence and polarization. However, 37 GHz data have a slightly stronger signal than the 19 GHz data, although it appears that there is a larger scatter in the 37 GHz data. The observed frequency sensitivity is consistent with the characteristics of microwave emission from self-similar rough surfaces with a roughness spectrum following the  $1/k^4$  power law for the length-scale of one to a few centimeters. Furthermore, a stronger signal at 37 GHz suggests that the surface spectrum rolls off at a slower rate than  $1/k^4$  in the wave number range of 300 to 700  $\text{rad m}^{-1}$ . The slower roll-off rate suggested by the WINDRAD data appears to be consistent with the wave tank measurements and theoretical analysis of small-scale wave spectra [17, 18].

Figures 5 and 6 plot  $T_{v1}$  and  $T_{v2}$  as a function of wind speed at  $45^\circ$ ,  $55^\circ$ , and  $65^\circ$

incidence angles, respectively for 19 and 37 GHz channels. The agreement between the WINDRAD data at  $55^\circ$  incidence angle and Wentz's SSM/I model function is reasonable.  $T_{v1}$  in general increases with increasing wind speed, and is larger at higher incidence angles. This is consistent with the fact that higher winds result in a less symmetric wave surface in the form of a skewness in surface slopes and an inhomogeneous distribution of capillary waves, breaking waves, and sea foam riding on the waves with a longer wavelength. Comparison of the data at these three incidence angles shows that the effects of upwind and downwind wave asymmetry are more pronounced at higher incidence angles. The magnitude of  $T_{v2}$  appears to be an increasing function of wind speeds, except at near  $55^\circ$  incidence angle. It appears that the sign of  $T_{v2}$  changes as the incidence angle varies between  $45^\circ$  and  $65^\circ$ . A phase transition will lead to a small magnitude of  $T_{v2}$  at  $55^\circ$  incidence angle. This phase transition is consistent with the signature of Bragg scattering by short-gravity and capillary waves [10] for vertically polarized radiation, which has a positive (negative) sensitivity to surface roughness at an incidence angle smaller (greater) than about  $55^\circ$  [16].

Figures 7 and 8 plot  $T_{h1}$  and  $T_{h2}$  versus wind speeds. Like  $T_{v1}$ ,  $T_{h1}$  is apparently larger at higher wind speeds and higher incidence angles. However,  $T_{h1}$  determined from aircraft data is several times smaller than  $T_{v1}$ , suggesting that the horizontally polarized radiation is less sensitive to surface wave asymmetry than the vertically polarized radiation. This characteristic is opposite to that of microwave ocean backscatter, but is consistent with the predictions of a two-scale scattering model with the wave-wave interaction mechanism [10, 11].

In comparison with Wentz's SSM/I model function, aircraft  $T_{h1}$  at near  $55^\circ$  incidence angle is significantly lower than that of Wentz's SSM/I  $T_{h1}$ . The cause of this discrepancy is unclear. Because cloudy sky data were excluded for the calculation of aircraft  $T_{h1}$  data, it is unlikely that atmospheric attenuation could have significantly altered the magnitudes of aircraft  $T_{h1}$  measurements. Since the second Stokes parameter  $Q$  is less sensitive to atmosphere than  $T_v$  and  $T_h$ ,  $Q_1$  and  $Q_2$  are plotted against the wind speed in Figures 9 and 10. The agree-

ment between aircraft and SSM/I  $Q_2$  is reasonable, but the disagreement between aircraft  $Q_1$  and Wentz's SSM/I  $Q_1$  remains quite large. A possible cause of discrepancy is the difference between satellite and aircraft antenna footprints with SSM/I footprints more than one order of magnitude greater than aircraft radiometer footprints. A larger area should result in a smaller anisotropic azimuth modulation] of brightness temperatures, because the variability of wind directions within the satellite radiometer footprint may smooth out the signals from sub-pixels. Nevertheless, the agreement between WINDRAD and Wentz's SSM/I model for  $T_{v1}$ ,  $T_{v2}$ ,  $T_{h2}$ , and  $Q_2$  suggests that the difference in footprint size may not be critical. Other factors, such as geographical and seasonal variations, need to be explored to explain this discrepancy.

$U_1$  and  $U_2$  are illustrated in Figures 11 and 12 for all sky conditions. Because  $U$  is fairly insensitive to clouds, it is possible to include the data for the wind speeds of about  $15\text{-}18\text{ m}\cdot\text{s}^{-1}$  acquired in November 1996 when there were stratus clouds over the buoy. The magnitude of  $U_1$  increases with increasing wind speed. This trend is consistent with the wind speed sensitivity of  $T_{v1}$ ,  $T_{h1}$ , and  $Q_1$ . The  $U_2$  data at  $45^\circ$  incidence angle show a monotonic increasing trend from low to moderate wind speeds, but appear to level off and even decrease above  $12\text{ m}\cdot\text{s}^{-1}$  wind speed. This characteristic has been suggested by limited SRI'S nadir viewing measurements [3, 4] at high winds ( $> 10\text{ m}\cdot\text{s}^{-1}$ ). As indicated by the simulation of a sea surface scattering model [10, 11], the sensitivities of sea surface brightness temperatures to winds at low to moderate incidence angles are dominated by the Bragg scattering by short waves. Since the wave spectrum study [17, 18] indicates that the directional spectra of short-gravity and capillary waves saturate and become more isotropic at high winds due to the short-wave dissipation induced by wave-drift interactions, the wind speed dependence of  $U_2$  data at  $45^\circ$  and  $55^\circ$  incidence angle appears to support previous studies of short-scale wave spectra.

An important feature of  $U_2$  at  $65^\circ$  incidence angle illustrated in Figures 11 and 12 is that  $U_2$  does not decrease monotonically as the wind speed decreases to zero. Data from several

flights indicate a 0.3-0.6 Kelvin signal in  $U_2$  within the wind speed range of 2-4  $\text{m}\cdot\text{s}^{-1}$  at  $65^\circ$  incidence angles. Figure 14 plots the 37 GHz  $U$  data versus  $\phi$  for these cases. These signals, although small, appear to be repeatable. (Part of the data scatter should be due to the uncertainty of buoy wind speed and direction measurements.) The exact cause of the low wind  $U_2$  data is unknown. During those flights, there were clouds over the buoys. Therefore, it is possible that these signals were caused by the reflected downwelling cloud radiation. However, the cloud layers were expected to be thin for three of the five cases because the estimated attenuation indicated in Figure 4 for these cases is less than the attenuation by the US standard atmosphere shown in Table 1. This suggests that the reflected cloud radiation may not be the source of low wind signals. Table 2 summarizes buoy measurements for these five cases. The surface temperatures indicate that the surfaces were stable or close to neutrally stable conditions. Three of the five cases have a small significant wave height (SWH), while two of them with SWH near 4 m might have swell around the buoys. There is no clear correlation between the low wind  $U_2$  at  $65^\circ$  incidence angle with these buoy measurements. Additionally, because sea foam and breaking waves are usually not present on the sea surface at low winds, the wind direction signal in  $U$  at low winds are likely to be caused by other mechanisms, such as shadowing and multiple scattering by long waves, which have more significant effects at high incidence angles.

The fourth Stokes parameter  $V$ , which signifies the circularly polarized components in the microwave radiation, has been acquired by the 19 GHz radiometer channel for several flights. Figure 13 illustrates  $V_1$  and  $V_2$  at three incidence angles. The signals, although weaker than  $U$ , remain distinct at moderate and high winds, even for cloudy skies. The upwind and downwind asymmetry of  $V$  is essentially zero at  $45^\circ$  incidence angle and slightly larger than zero at higher incidence angles.  $V_2$  increases monotonically with wind speed and is stronger at higher incidence angles. Just like  $U$ , the data suggest that  $V_2$  also saturates at high winds.

As suggested by [5], one of the sea surface features that may contribute to the azimuthal

variations of brightness temperatures is the sea foam, which distribute unevenly on the leeward and windward faces of the ocean waves. The fractional area ( $A_f$ ) of sea foam over sea surfaces is a function of wind speed and atmospheric stability. Many experimental studies [19] have shown that  $A_f$  can be approximately related to the wind speed at 10 m elevation ( $U_{N10}$ ) by a power law:  $A_f = \beta U_{N10}^\gamma$  with the exponent  $\gamma$  in the range of 2.5 to 3.5. This relation appears to be valid for  $U_{N10}$  up to  $20 \text{ m}\cdot\text{s}^{-1}$  based on the experimental data illustrated in Figure 9 [19]. If the azimuth variations of brightness temperatures are dominated by the sea foam, then the amplitudes of azimuth brightness variations could be proportional to  $A_f$  and increases approximately cubically with increasing wind speed. However, none of the first and second harmonic coefficients from the WINDRAD flights, Wentz's SSM/I model function and SRI's data has shown such a wind speed dependence. This suggests that either sea foam may become more isotropically distributed at high winds or other surface wave features may have a stronger influence on the azimuthal variations of brightness temperatures.

As suggested by the data illustrated in Figures 5 to 13, indicating a rapid increase of directional signals at low winds and a slower increase or saturation at high winds, the following exponential function was selected to fit the Fourier coefficients as a function of  $U_{N195}$ :

$$f(U_{N195}) = c_1[1 - e^{-(U_{N195}/a_1)^{\alpha_1}}] + c_2[1 - e^{-(U_{N195}/a_2)^{\alpha_2}}] \quad (16)$$

To model the low wind bumps of  $U_2$  at  $65^\circ$  incidence angle, the second term with the same functional form was included in  $f(U_{N195})$  for  $U_2$ .

Tables 3 and 4 summarize the model coefficients for the empirical curves (thick solid and dashed lines) illustrated in Figures 5 to 13. A larger upwind and downwind asymmetry at higher incidence angles is clearly indicated in the magnitudes of the first harmonic coefficients versus incidence angles. In general, the empirical curves fit the data reasonably well, except a few outliers. For example, two  $U_1$  measurements from two consecutive sets of flight circles at a wind speed near  $11 \text{ m/s}$  in the bottom panel of Figure 12 were acquired over a coastal

NDBC buoy (ID number *46027*) located near St. George, northern California and are more than two times larger than the other  $U_1$  data measured at about the same wind speeds. Similar outliers can be found in the data acquired from the same set of circle flights at the other incidence angles. (Because the K-band radiometer was commanded to take  $V$  measurements for one of the two sets of circles, only the outlier at a wind speed of about 10.5 m/s can be seen in Figure 1 1.) This suggests that other oceanic parameters in addition to wind speed may play a critical role in determining the magnitude of wind direction signals in sea surface brightness temperatures. Nevertheless, most data points can be modeled fairly well by the empirical curves.

## 5 Summary

The polarimetric microwave sea surface brightness temperatures acquired by the JPL aircraft WINDR AD flights from 1994 through 1996 were reduced to a set of cosine and sine series coefficients. These coefficients were plotted as a function of wind speed for each frequency, incidence angle and Stokes parameter. The wind direction signals have a broad frequency spectrum from 19 to 37 GHz, although the 37-GHz channel provides a stronger direction signal than the 19-GHz channel. The upwind and downwind asymmetries of all Stokes parameters increase with increasing wind speed or incidence angle, while the characteristics of upwind and crosswind asymmetries are strongly dependent on polarization and incidence angle.

An empirical model function is proposed and is shown to fit the data reasonably well. There are a few outliers acquired over a coastal moored buoy. The ancillary data including SWH and surface temperatures for those outliers appear to be very similar to the other points at about the same wind speeds. This indicates that other oceanic processes and parameters, such as internal waves in addition to surface wind velocities may play an important role in determining the strength of azimuthal modulations of short-gravity and capillary waves.

## **6 Acknowledgment**

This work was ~m-formed under contract with the National Aeronautics and Space Administration at the Jet Propulsion Laboratory, California Institute of Technology. The authors would like to thank the DC-8 aircraft flight crew of the NASA Ames Research Center and the P-3 aircraft flight crew of the NASA Wallops Flight Facility for assistance in aircraft flight planning and experiments.



## References

- [1] I. Tsang, "Polarimetric passive remote sensing of random discrete scatterers and rough surfaces," *J. Electromagnetic Waves and Appl.*, Vol. 5, No. 1, 41-57, 1991.
- [2] J. P. Hollinger, J. L. Peirce, and G. A. Poe, "SSM/Instrument evaluation," *IEEE Trans. Geosci. Remote Sensing*, Vol. 28, No. 5, 781-790, Sep., 1990.
- [3] V. S. Etkin, M.D. Raev, M.G. Bulatov, Yu.A. Militsky, A.V. Smirnov, V.Yu. Raizer, Yu.A. Trokhimovsky, V.G. Irisov, A.V. Kuzmin, K.Ts. Litovchenko, E. A. Bespalova, E.I. Skvortsov, M.N. Pospelov, and A.J. Smirnov, *Radiohydrophysical Aerospace Research of Ocean*, Report IIP-1749, Academy of Sciences, Space Research Institute, Moscow, USSR, 1991.
- [4] V. G. Irisov, A. V. Kuzmin, M. N. Pospelov, J. G. Trokhimovsky, and V. S. Etkin, "The dependence of sea brightness temperature on surface wind direction and speed. Theory and Experiment .," *IEEE, Proceedings of International Geoscience and Remote Sensing Symposium*, Houston, 1992.
- [5] F. J. Wentz, "Measurement of oceanic wind vector using satellite microwave radiometers," *IEEE Trans. Geosci. Remote Sensing*, Vol. 30, No. 5, 960-972, Sep., 1992.
- [6] M. S. Dzura, V. S. Etkin, A. S. Khrupin, M. N. Pospelov, and M. D. Raev, "Radiometers-polarimeters: principles of design and applications for sea surface microwave emission polarimetry," *Proceedings of International Geoscience and Remote Sensing Symposium*, Houston, 1992.
- [7] S. H. Yueh, W. J. Wilson, F.K. Li, W. B. Ricketts, and S. V. Nghiem, "Polarimetric measurements of sea surface brightness temperatures using an aircraft K-band radiometer," *IEEE Trans. Geosci. Remote Sensing*, Vol. 33, No. 1, 85-92, 1995.
- [8] S. H. Yueh, W. J. Wilson, F. K. Li, W. B. Ricketts, and S. V. Nghiem, "Polarimetric brightness temperatures of sea surfaces measured with aircraft K- and Ka-band radiometers," *IEEE Trans. Geosci. Remote Sensing*, Vol. 35, No. 5, 1997.
- [9] John D. Kraus, *Radio Astronomy*, 2nd. ed., 1986, Cygnus-Quasar Books, Powell, Ohio.
- [10] S. H. Yueh, "Modelling of Wind Direction Signals in Polarimetric Sea Surface Brightness Temperatures," *IEEE Trans. Geosci. Remote Sensing*, November 1997.
- [11] P. Coppo, J. T. Johnson, L. Guerriero, J. A. Kong, G. Macelloni, F. Marzano, P. Pampaloni, N. Pierdicca, D. Solimini, C. Susini, G. Tofani, and Y. Zhang, *Polarimetry For Passive Remote Sensing*, Final Report for European Space Agency Contract N° 11446/95/NL/Nil, Centro di Telerilevamento a Microonde, Firenze, Italy, 1 December 1996.
- [12] W. G. Large and S. Pond, "Open ocean momentum flux measurements in moderate to strong winds," *J. Phys. Oceanogr.*, 11, 324-336, 1981.
- [13] W. T. Liu and W. Tang, "Equivalent Neutral Wind," Jet Propulsion Laboratory Publication 96-17, August 1, 1996.

- [14] S. H. Yueh, R. Kwok, and S. V. Nghiem, "Polarimetric scattering and emission properties of targets with reflection symmetry," *Radio Science*, Vol. 29, No. 6, 1409-1420, November-December, 1994.
- [15] W. H. Peake, "Interaction of electromagnetic waves with some natural surfaces," *IEEE Trans. Ant. and Prop.*, Vol. AP-7, spec. suppl. 8324-8329, 1959.
- [16] J. P. Hollinger, "Passive microwave measurements of sea surface roughness," *IEEE Trans. Geosci. Electronics*, Vol. GE-9, No. 3, 165-169, July 1971.
- [17] Bernd Jahne and Klaus S. Riemer, "Two-Dimensional Wave Number Spectra of Small-Scale Surface Waves," *J. Geophys. Res.* Vol. 95, No. C7, 11,531-11,546, July 1990.
- [18] Yuguang Liu and Xiao-H. Yau, "The Wind-Induced Wave Growth Rate and the Spectrum of the Gravity-Capillary Waves," *J. of Phy. Oceanography*, Vol. 25, 3196-3218, December 1995.
- [19] E. C. Monahan and I. G. O'Muircheartaigh, "Whitecaps and the passive remote sensing of the ocean surface," *Int. J. Remote Sensing* Vol. 7, No. 5, 627-642, 1986.
- [20] H. J. Liebe, "An updated model for millimeter wave propagation in moist air," *Radio Science*, Vol. 20, No. 5, 1069-1089, 1985.
- [21] Wentz, Frank J., S. Peteherych, and L. A. Thomas, "A model function for ocean radar cross sections at 14.6 GHz," *Journal of Geophysical Research*, Vol. 89, No. C3, 3689-3704, 1984.

## List of Tables

1	Effects of atmosphere at $55^\circ$ incidence angle. $\alpha$ and atmospheric radiation ( $T_U, T_D$ ) are calculated using Liebe's millimeter wave propagation model for US standard atmosphere. $T_s$ is 285 Kelvin. . . . .	20
2	Summary of key buoy measurements at low winds during WINDRAD flights. W is the buoy wind speed at 5 m elevation and SST is the sea surface temperature. $U_{N195}$ is the equivalent neutral wind at 19.5 m elevation calculated from buoy measurements based on [12]. . . . .	21
3	The coefficients of the exponential model function at 19.35 GHz. . . . .	22
4	The coefficients of the exponential model function at 37 GHz. . . . .	23

Frequency (GHz)	$\alpha$ (dB)	$T_U, T_D$ (K)	A	A (dB)	B
19.35	-0.35	23	0.85	-0.7	44
37	-0.54	34	0.77	-1.1	64

Table 1: Effects of atmosphere at 55° incidence angle.  $\alpha$  and atmospheric radiation ( $T_U, T_D$ ) are calculated using Liebe's millimeter wave propagation model for US standard atmosphere.  $T_s$  is 285 Kelvin.

Data ID	W (m/s)	$U_{N195}$ (m/s)	Air Temperature ( $^{\circ}\text{C}$ )	SST ( $^{\circ}\text{C}$ )	SWH (m)
08012026	2.2	2.5	14.3	12.9	1.1
05242011	2.9	3.4	13.3	13.6	1.3
05242116	3.1	3.7	13.4	13.7	1.3
09222114	2.9	3.5	18.0	19.1	4.2
09222257	3.7	4.4	18.1	18.9	4.0

Table 2: Summary of key buoy measurements at low winds during WINDRAD flights. W is the buoy wind speed at 5 m elevation and SST is the sea surface temperature.  $U_{N195}$  is the equivalent neutral wind at 19.5 m elevation calculated from buoy measurements based on [12].

Parameter	$\theta$	$c_1$	$a_1$	$\alpha_1$	$c_2$	$a_2$	$\alpha_2$
$T_{v1}$	45	3.1	15	2	0	-	-
$T_{h1}$	45	-0.2	15	2	0	-	-
$U_1$	45	-2.8	15	2	0	-	-
$V_1$	45	0.1	10	-2	0	-	-
$T_{v2}$	45	2.1	15	1.8	0	-	-
$T_{h2}$	45	-1.4	7	3	0	-	-
$U_2$	45	-2.3	7	3	0.6	25	1.8
$V_2$	45	0.8	7	4	0	-	-
$T_{v1}$	55	3.8	13	2	0	-	-
$T_{h1}$	55	0.6	13	-2	0	-	-
$U_1$	55	-3.5	13	2	0	-	-
$V_1$	55	0.4	-10	2	0	-	-
$T_{v2}$	55	0.0	15	1.4	0	-	-
$T_{h2}$	55	-1.5	7	3	0	-	-
$U_2$	55	-1.9	7	3	2.0	25	1.4
$V_2$	55	0.9	7	4	0	-	-
$T_{v1}$	65	3.4	12	2	0	-	-
$T_{h1}$	65	1.2	12	2	0	-	-
$U_1$	65	-3.1	12	2	0	-	-
$V_1$	65	0.3	10	2	0	-	-
$T_{v2}$	65	-2.5	12	1.0	0	-	-
$T_{h2}$	65	-1.1	6	3	0	-	-
$U_2$	65	-2.7	6	3	5.0	12	1.0
$V_2$	65	1.1	7	5	0	-	-

Table 3: The coefficients of the exponential model function at 19.35 GHz.

Parameter	$\theta$	$c_1$	$a_1$	$\alpha_1$	$c_2$	$a_2$	$\alpha_2$
$T_{v1}$	45	3.2	11	2	0	-	-
$T_{h1}$	45	0.4	11	2	0	-	-
$U_1$	45	-2.9	11	2	0	-	-
$T_{v2}$	45	1.4	15	1.8	0	-	-
$T_{h2}$	45	-2.0	7	3	0	-	-
$U_2$	45	-2.2	7	3	0.7	25	1.8
$T_{v1}$	55	3.8	10	2	0	-	-
$T_{h1}$	55	1.2	10	2	0	-	-
$U_1$	55	-3.8	10	2	0	-	-
$T_{v2}$	55	-1.1	15	1.4	0	-	-
$T_{h2}$	55	-2.1	7	3	0	-	-
$U_2$	55	-1.6	7	3	2.3	25	1.4
$T_{v1}$	65	3.1	9	2	0	-	-
$T_{h1}$	65	1.7	9	2	0	-	-
$U_1$	65	-3.1	9	2	0	-	-
$T_{v2}$	65	-3.3	12	1.0	0	-	-
$T_{h2}$	65	-1.9	6	3	0	-	-
$U_2$	65	-1.9	6	3	4.4	12	1.0

~'able 4: The coefficients of the exponential model function at 37 GHz.

## List of Figures

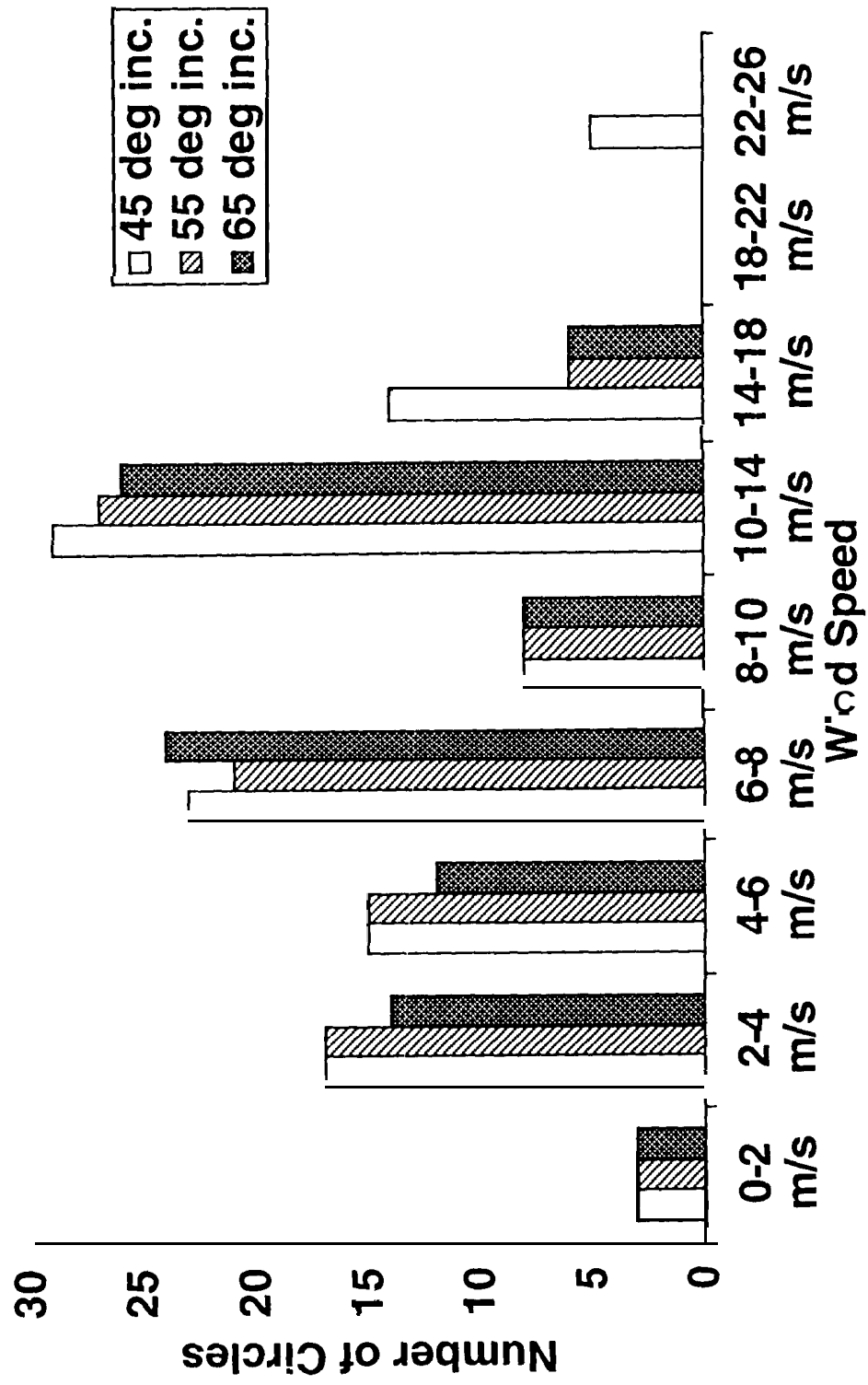
- 1 Summary of aircraft WINDRAD flight circles over NOAA NDBC buoys from 1993 through 1996 at  $45^\circ$ ,  $55^\circ$ , and  $65^\circ$  incidence angles. . . . . 28
- 2 Wind direction signals in polarimetric brightness temperatures of ocean surfaces acquired by JPL K- and Ka-band radiometers at  $55^\circ$  incidence angle. The data were acquired on 17 April 1995 with NASA DC-8 flights over NDBC buoy 46005. The skies were mostly clear with some small scattered clouds. The buoy wind speed is  $8.9 \text{ m}\cdot\text{s}^{-1}$  at 5 m elevation, which corresponds to  $9.6 \text{ m}\cdot\text{s}^{-1}$  at 10 m elevation and  $10.1 \text{ m}\cdot\text{s}^{-1}$  at 19.5 m elevation based on the correction of a boundary layer model [12]. For ease of comparison,  $T_v$ ,  $T_h$ , and  $Q$  at 19.35 GHz have been offset by 187.5, 119.3, and 68.2 Kelvin, respectively, while those at 37 GHz have been offset by 203.9, 136.8, and 67.1 Kelvin. . . 29
- 3 Polarimetric brightness temperatures of ocean surfaces acquired by JPL K-band radiometer at  $45^\circ$  incidence angle with thick stratus clouds over the buoy. The data were acquired on 22 September 1996 with NASA P-3 flights over NDBC buoy 41001. The buoy wind speed is  $15 \text{ m}\cdot\text{s}^{-1}$  at 5 m elevation. The upper pane] plots the Ku-band VV backscatter measured by a Ku-band (13.995 GHz) scatterometer at the same time and the prediction by the geophysical mode] function for Seasat scatterometer [21] at an incidence angle of  $300^\circ$ . . . . . 30
- 4 Estimates of atmospheric attenuation at 55 degree incidence angle . . . . . 31



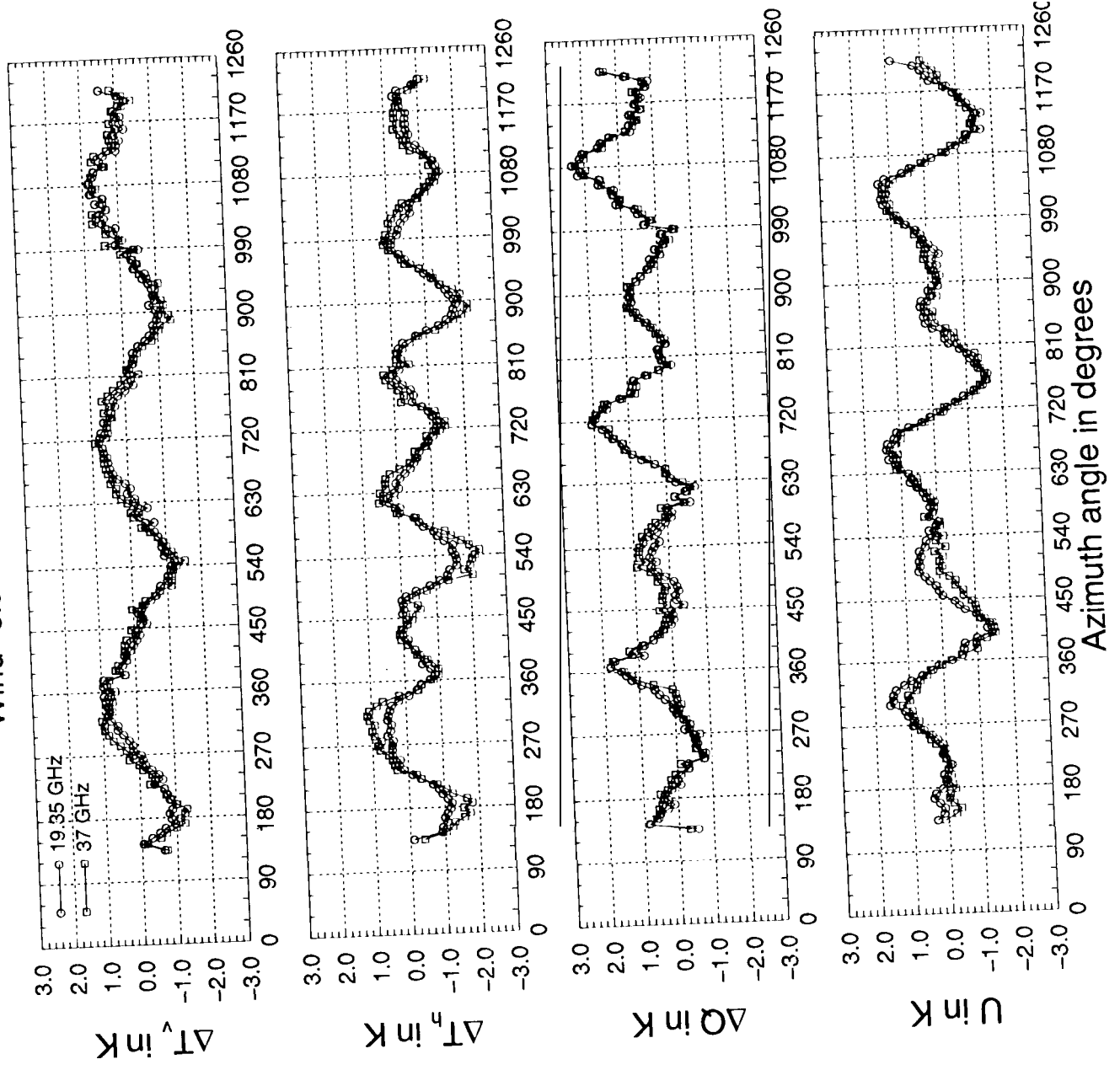
- 5  $T_{v1}$  and  $T_{v2}$  versus  $U_{N195}$  at 19.35 GHz. The upper panel is for  $45^\circ$  incidence angle, the middle panel for  $55^\circ$  incidence angle, and the lower panel for  $65^\circ$  incidence angle. Black dots and open rectangles represent coefficients reduced from experimental data. Thick solid and dashed lines are the outputs of the empirical exponential model. Thin solid and dashed lines in the middle panel are the predictions of Wentz's SSM/I model function. Only data acquired under clear skies are presented due to the large sensitivity of  $T_v$  to clouds. Buoy wind speed was converted to that at 19.5 m elevation based on [12]. . . . 32
- 6  $T_{v1}$  and  $T_{v2}$  versus  $U_{N195}$  at 37 GHz. The upper panel is for  $45^\circ$  incidence angle, middle panel for  $55^\circ$  incidence angle, and lower panel for  $65^\circ$  incidence angle. Black dots and open rectangles represent coefficients reduced from experimental data. Thick solid and dashed lines are the outputs of the empirical exponential model. Thin solid and dashed lines in the middle panel are the predictions of Wentz's SSM/I model function. Only data acquired under clear skies are presented due to the large sensitivity of  $T_v$  to clouds. Wind speed was converted to 19.5 m elevation based on [12]. . . . . 33
- 7  $T_{h1}$  and  $T_{h2}$  versus  $U_{N195}$  at 19.35 GHz. The upper panel is for  $45^\circ$  incidence angle, middle panel for  $55^\circ$  incidence angle, and lower panel for  $65^\circ$  incidence angle. Black dots and open rectangles represent coefficients reduced from experimental data. Thick solid and dashed lines are the outputs of the empirical exponential model. Thin solid and dashed lines in the middle panel are the predictions of Wentz's SSM/I model function. Only data acquired under clear skies are presented due to the large sensitivity of  $T_h$  to clouds. Buoy wind speed was converted to that 19.5 m elevation based on [12]. . . . . 34

8	$T_{h1}$ and $T_{h2}$ versus $U_{N195}$ at 37 GHz. The upper panel is for $45^\circ$ incidence angle, middle panel for $55^\circ$ incidence angle, and lower panel for $65^\circ$ incidence angle. Black dots and open rectangles represent coefficients reduced from experimental data. Thick solid and dashed lines are the outputs of the empirical exponential model. are the predictions of Wentz's SSM/I model function. Only data acquired under clear skies are presented due to the large sensitivity of $T_h$ to clouds. Buoy wind speed was converted to that 19.5 m elevation based on [12] . . . . .	35
9	$Q_1$ and $Q_2$ versus $U_{N195}$ at 19.35 GHz. The upper panel is for $45^\circ$ incidence angle, middle panel for $55^\circ$ incidence angle, and lower panel for $65^\circ$ incidence angle. Black dots and open rectangles represent coefficients reduced from experimental data. Thick solid and dashed lines are the outputs of the empirical exponential model. Thin solid and dashed lines in the middle panel are the predictions of Wentz's SSM/I model function. Only data acquired under clear skies are presented due to the large sensitivity of $T_h$ to clouds. Buoy wind speed was converted to that 19.5 m elevation based on [12]. . . . .	36
10	$Q_1$ and $Q_2$ versus $U_{N195}$ at 37 GHz. The upper panel is for $45^\circ$ incidence angle, middle panel for $55^\circ$ incidence angle, and lower panel for $65^\circ$ incidence angle. Black dots and open rectangles represent coefficients reduced from experimental data. Thick solid and dashed lines are the outputs of the empirical exponential model. Thin solid and dashed lines in the middle panel are the predictions of Wentz's SSM/I model function. Only data acquired under clear skies are presented due to the large sensitivity of $T_h$ to clouds. Buoy wind speed was converted to that 19.5 m elevation based on [12]. . . . .	37

11	$U_1$ and $U_2$ versus $U_{N195}$ at 19.35 GHz. The upper panel is for $45^\circ$ incidence angle, middle panel for $55^\circ$ incidence angle, and lower panel for $65^\circ$ incidence angle. Black dots and open rectangles represent coefficients reduced from experimental data. Thick solid and dashed lines are the outputs of the empirical exponential model. Buoy wind speed was converted to that 19.5 m elevation based on [12] . . . . .	38
12	$U_1$ and $U_2$ versus $U_{N195}$ at 37 GHz. The upper panel is for $45^\circ$ incidence angle, middle panel for $55^\circ$ incidence angle, and lower panel for $65^\circ$ incidence angle. Black dots and open rectangles represent coefficients reduced from experimental data. Thick solid and dashed lines are the outputs of the empirical exponential model. Buoy wind speed was converted to that 19.5 m elevation based on [12] . . . . .	39
13	$V_1$ and $V_2$ versus $U_{N195}$ at 19.35 GHz. The upper panel is for $45^\circ$ incidence angle, middle panel for $55^\circ$ incidence angle, and lower panel for $65^\circ$ incidence angle. Black dots and open rectangles represent coefficients reduced from experimental data. Thick solid and dashed lines are the outputs of the empirical exponential model. Buoy wind speed was converted to that 19.5 m elevation based on [12] . . . . .	40
14	37 GHz measurements of U data versus azimuth angle at low winds at $65^\circ$ incidence angle. The legend indicates the equivalent neutral wind speed at 19.5 m elevation based on [12] for each of the five cases. . . . .	41

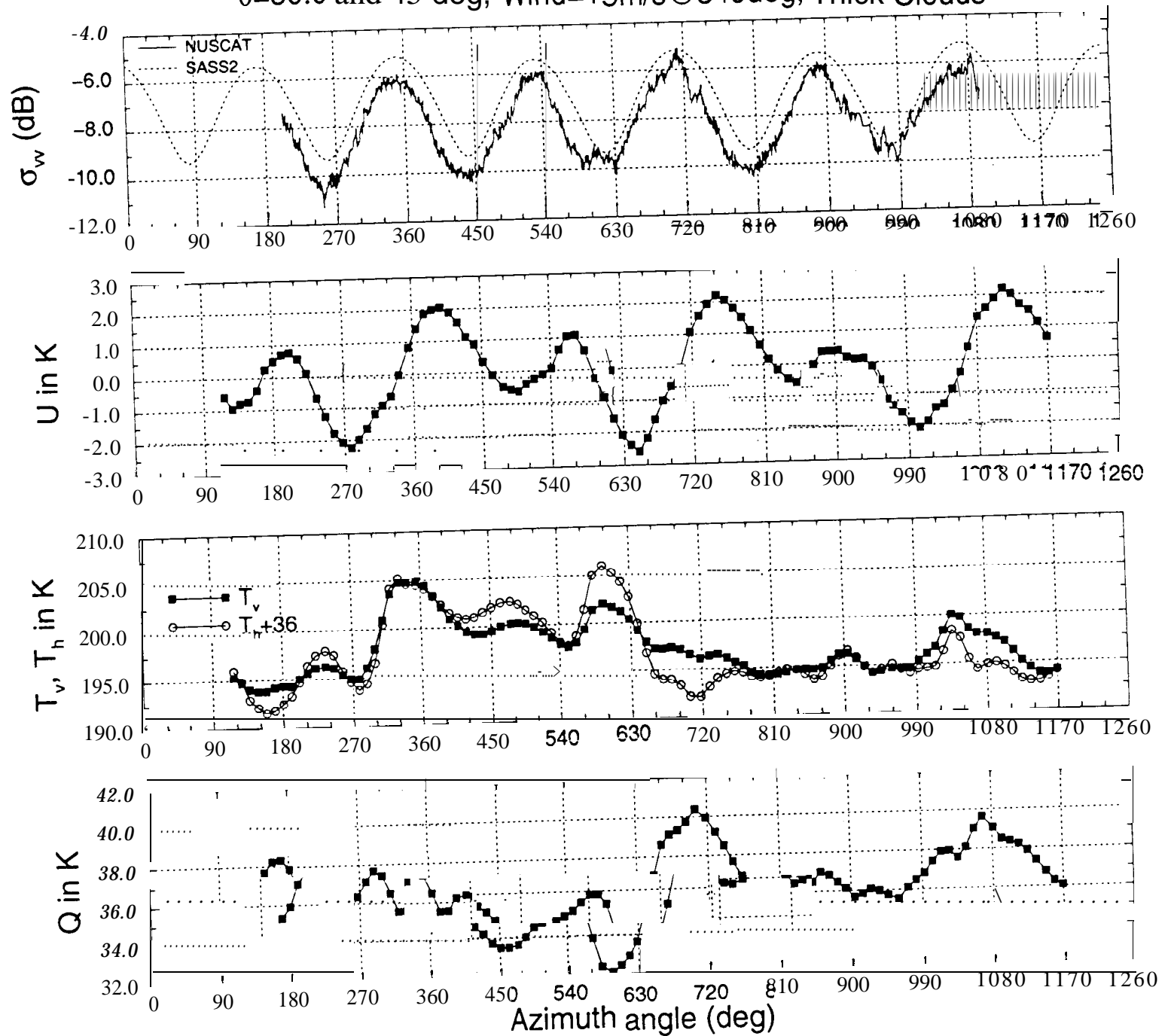


Wind=8.9 m/s@5m;  $\theta=55$  deg

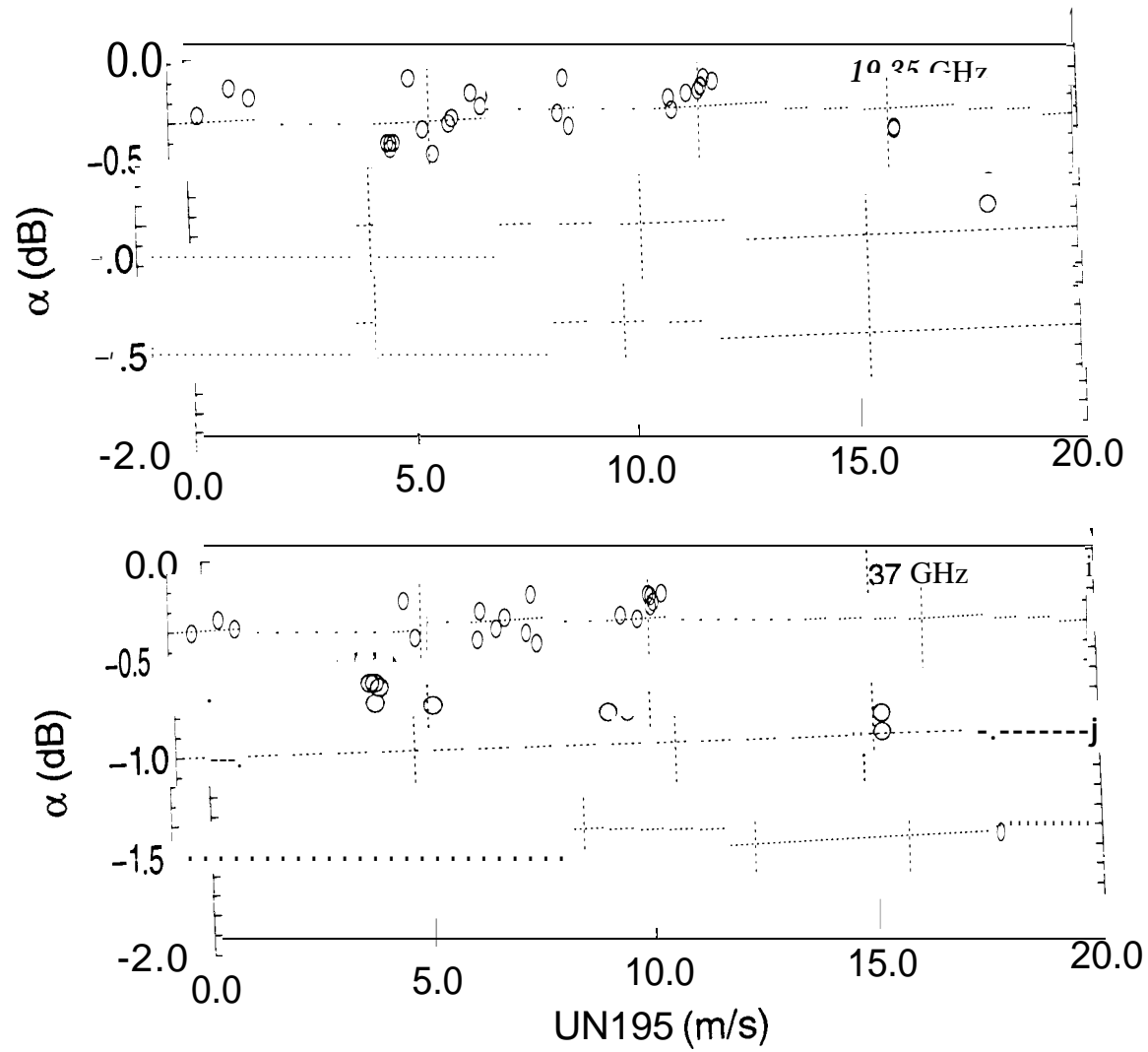


# JPL NUSCAT/WINDRAD 1996, 11221622

$\theta=30.0$  and  $45$  deg, Wind= $15\text{m/s}$ @ $340\text{deg}$ , Thick Clouds

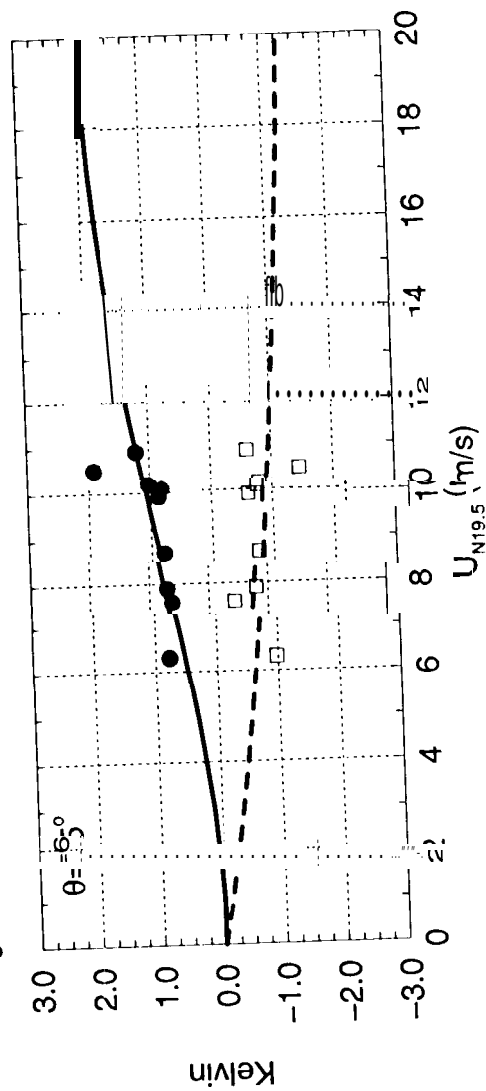
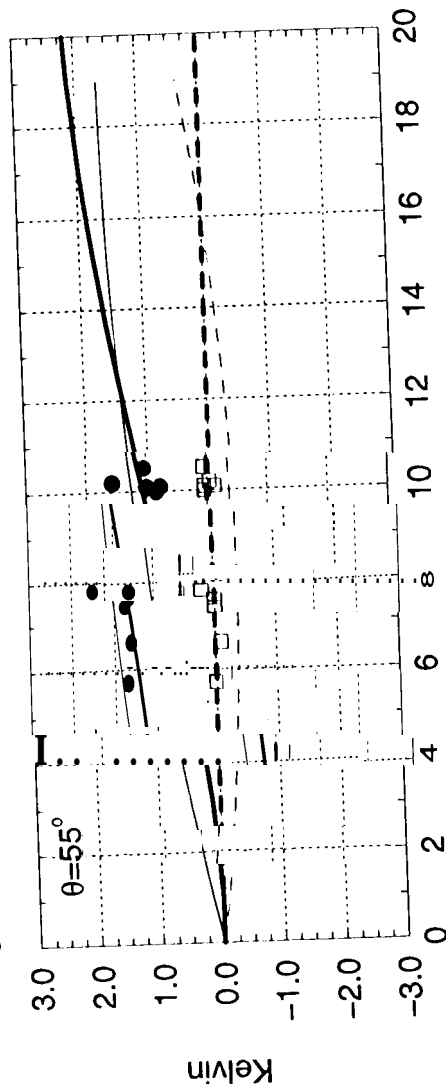
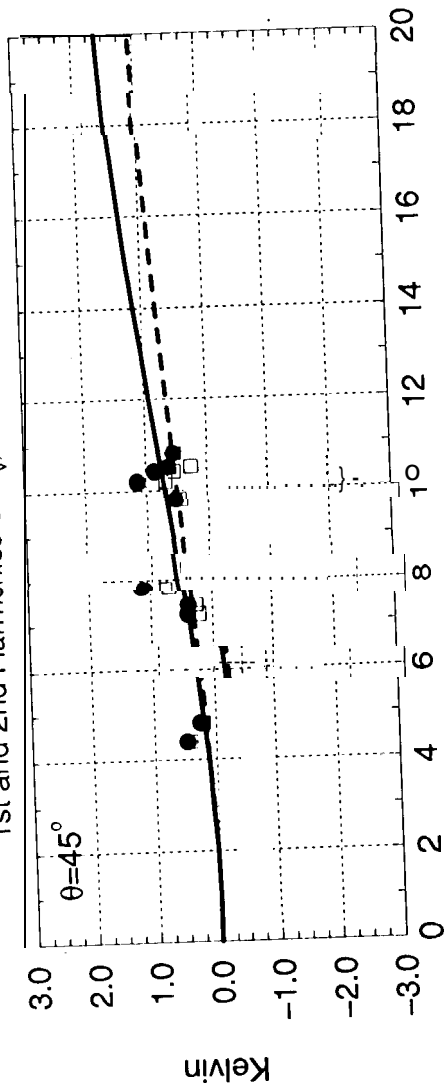


# ATMOSPHERIC TRANSMITTANCE



# 1993-1996 JPL WINDRAD DATA SUMMARY

1st and 2nd Harmonics of  $T_v$ , 19.35 GHz, Clear Sky



$\bullet$   $T_{v1}$   
 $\square$   $T_{v2}$   
 —  $T_{v1}$  curve fit  
 - -  $T_{v2}$  curve fit  
 — SSM/I  $T_{v1}$   
 - - SSM/I  $T_{v2}$



# 1993-1996 JPL WINDRAD DATA SUMMARY

1st and 2nd Harmonics of  $T_v$ , 37 GHz, Clear Sky

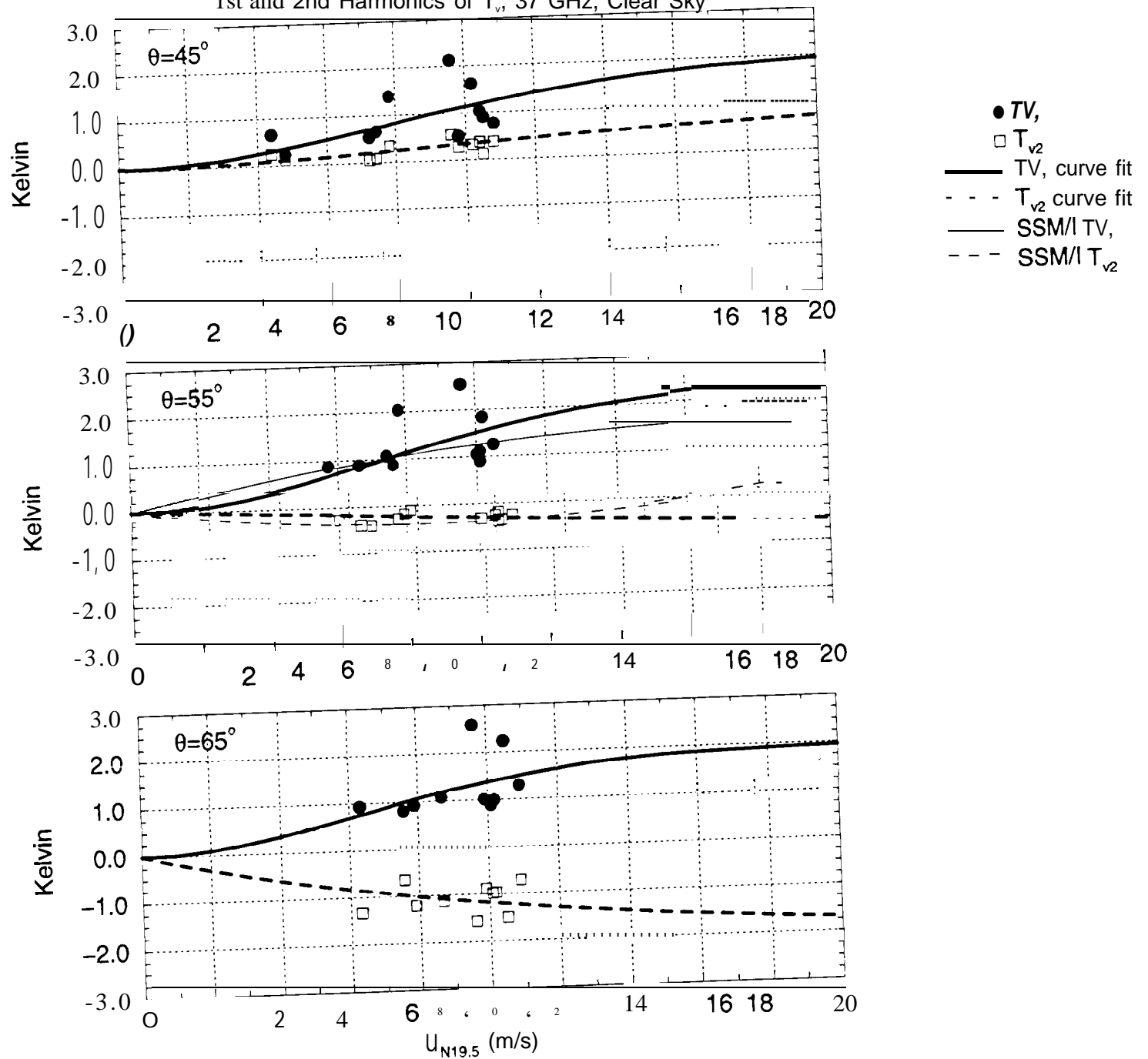
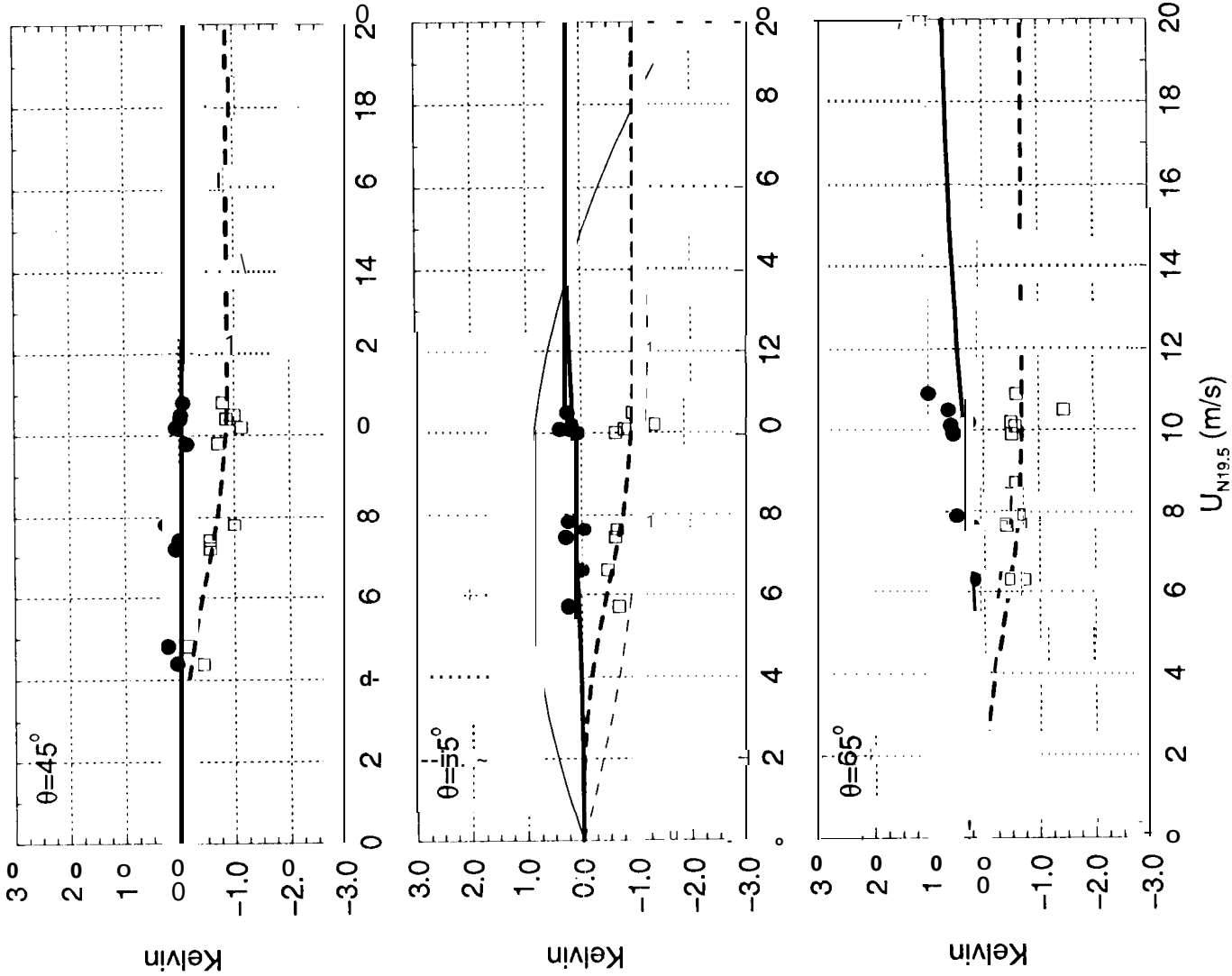


Fig 6

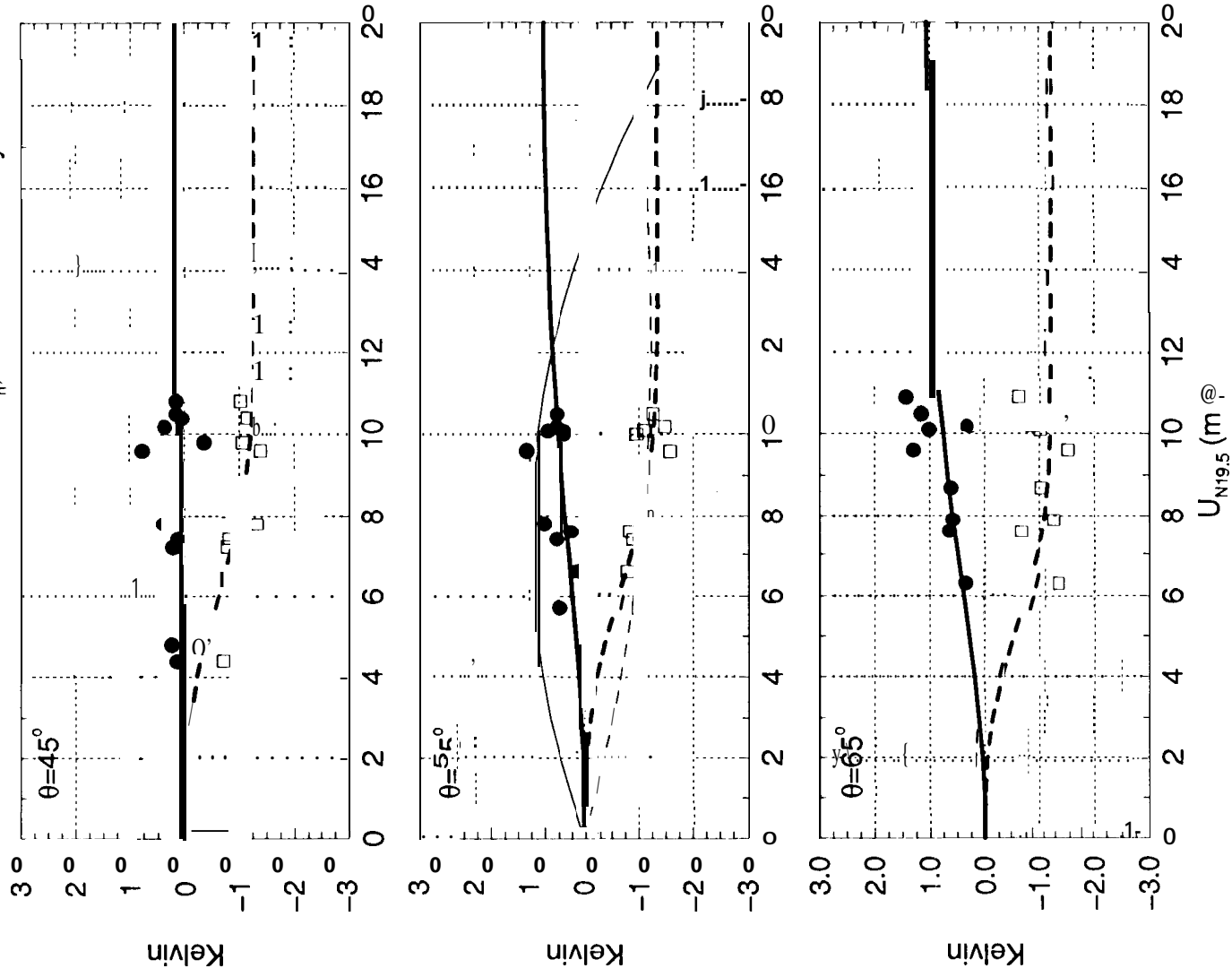
# 1993-1996 JPL WINDRAD DATA SUMMARY

1st and 2nd Harmonics of  $T_h$ , 19 GHz, Clear Sky



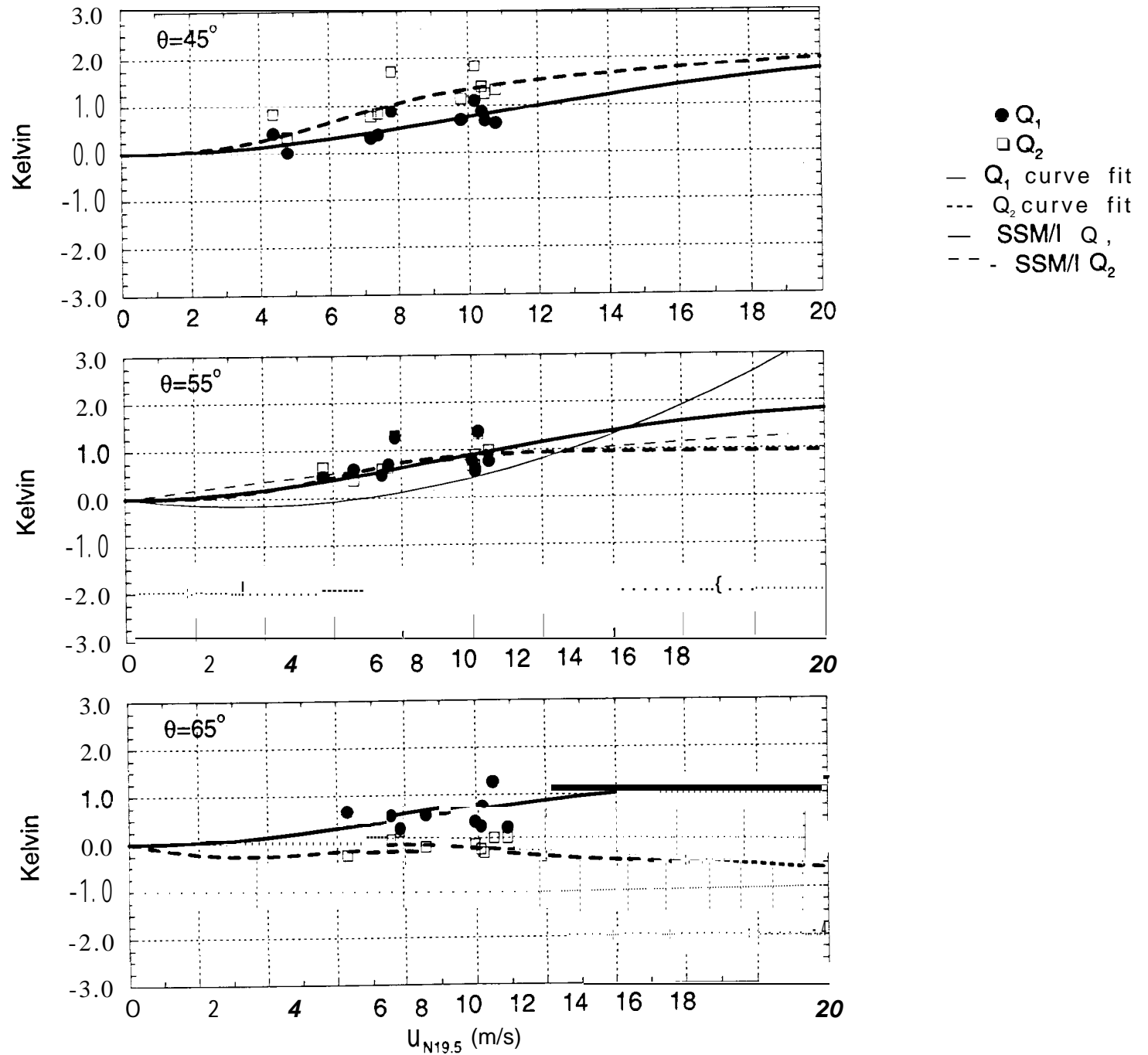
# 1993–1996 JPL WINDRAD DATA SUMMARY

1st and 2nd Harmonics of  $T_h$ , 37 GHz, Clear Sky



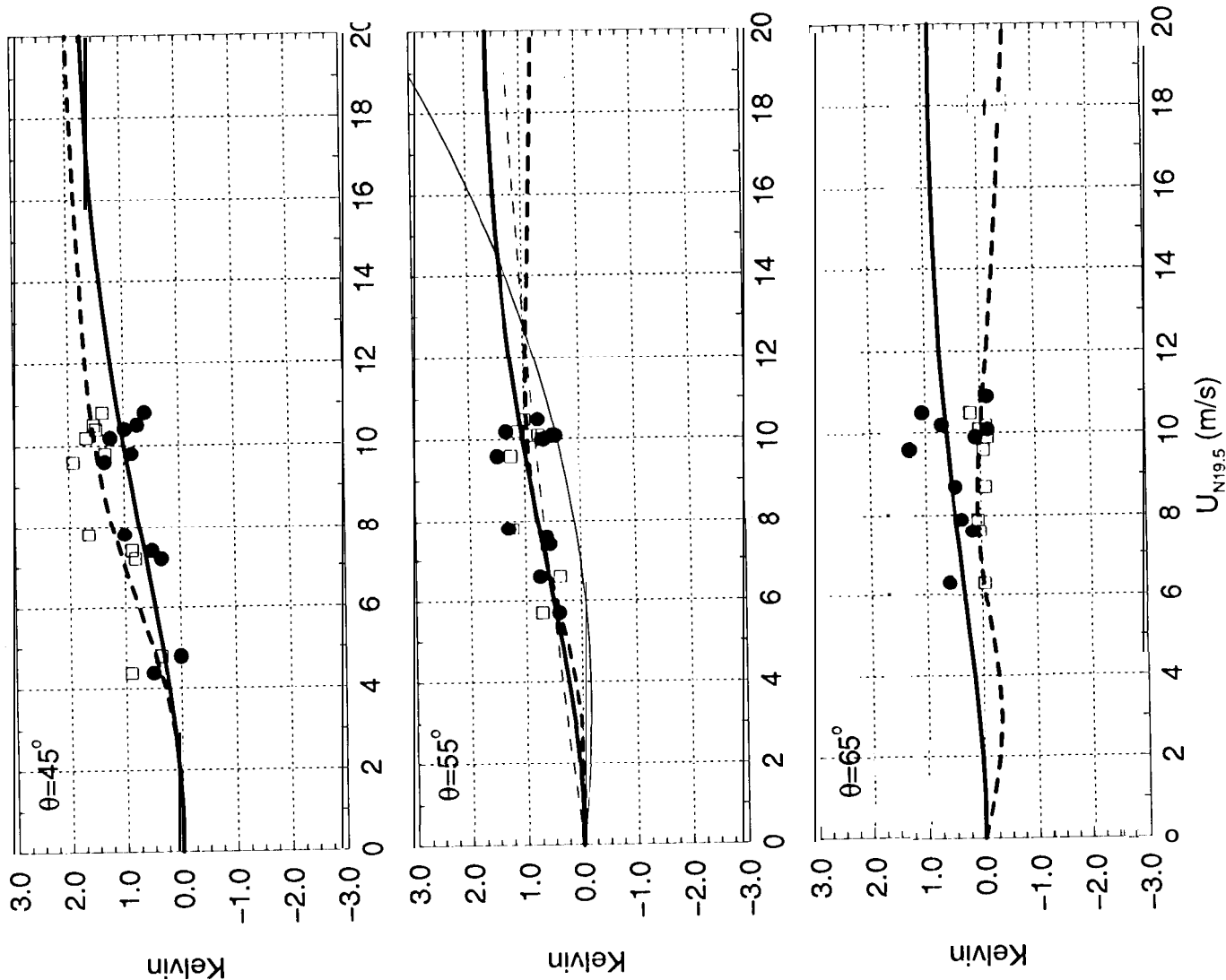
# 1993-1996 JPL WINDRAD DATA SUMMARY

1st and 2nd Harmonics of Q, 19.35 GHz, Clear Sky



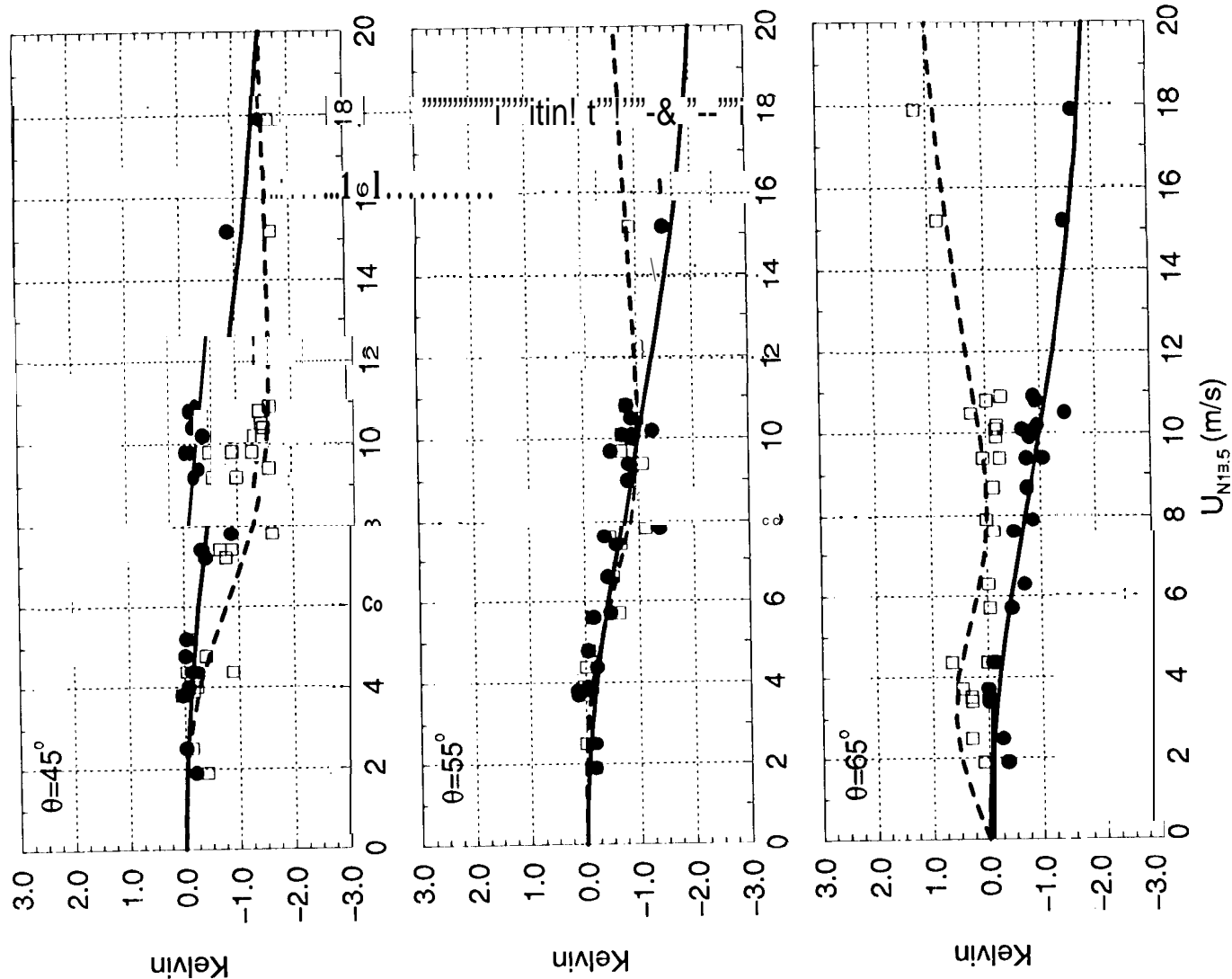
# 1993-1996 JPL WINDRAD DATA SUMMARY

1st and 2nd Harmonics of Q, 37 GHz, Clear Sky



# 993-1996 JPL WINDRAD DATA SUMMARY

1st and 2nd Harmonics of U, 19.35 GHz



# 1993-1996 JPL WI NDRAD DATA SUMMARY

1st and 2nd Harmonics of U, 37 GHz

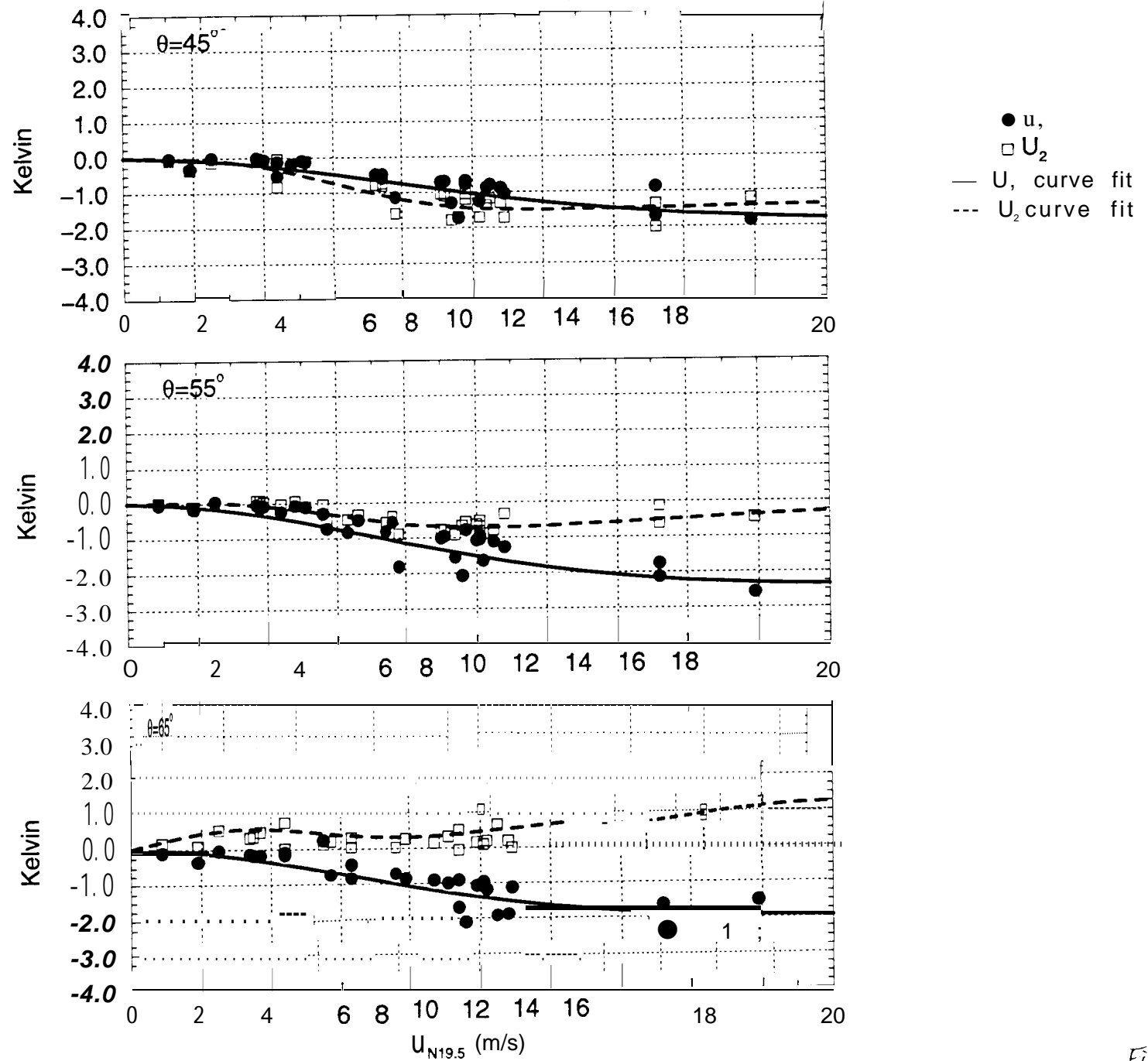
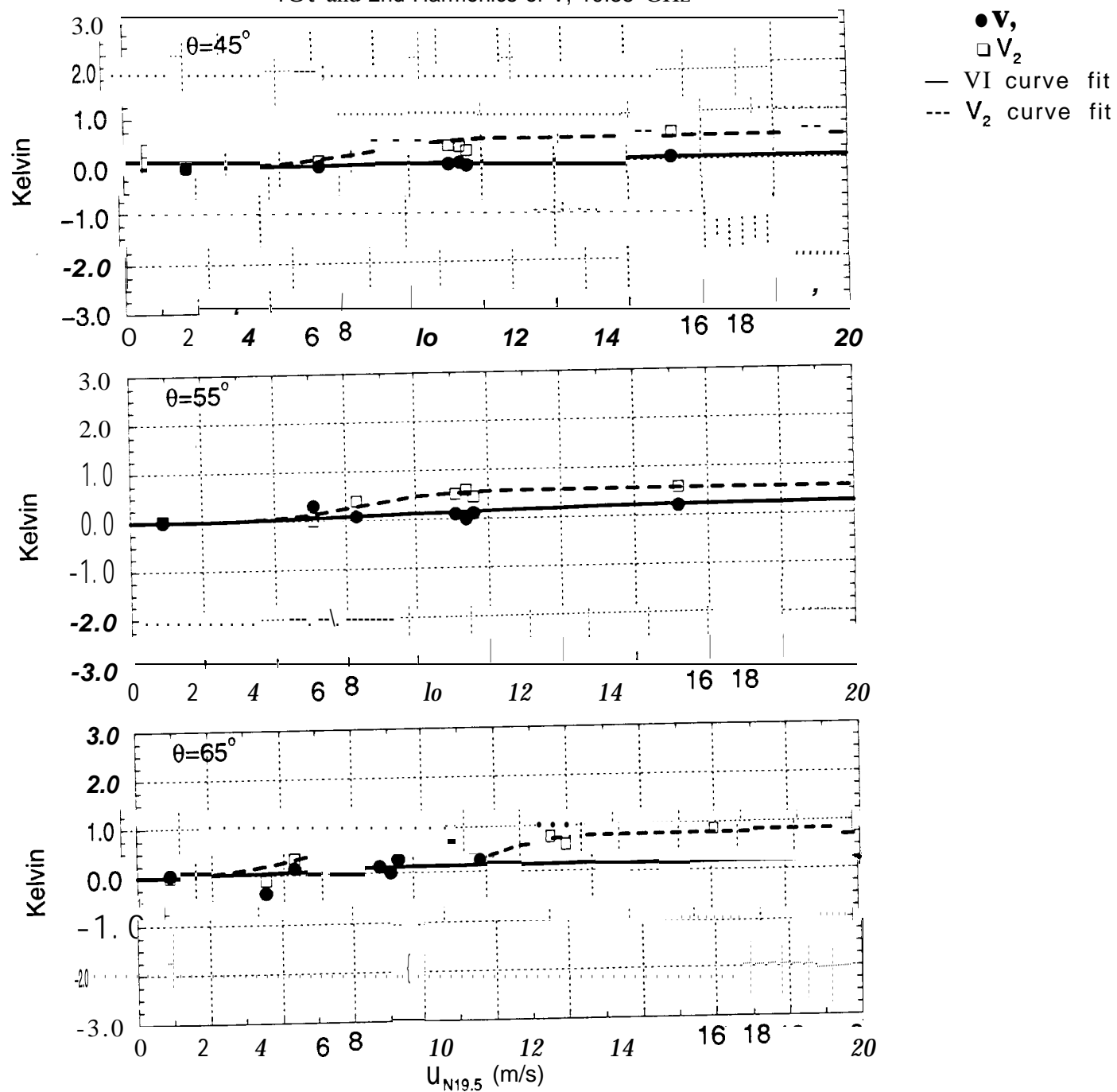


Fig 12

# 1993-1996 JPL WINDRAD DATA SUMMARY

1st and 2nd Harmonics of V, 19.35 GHz





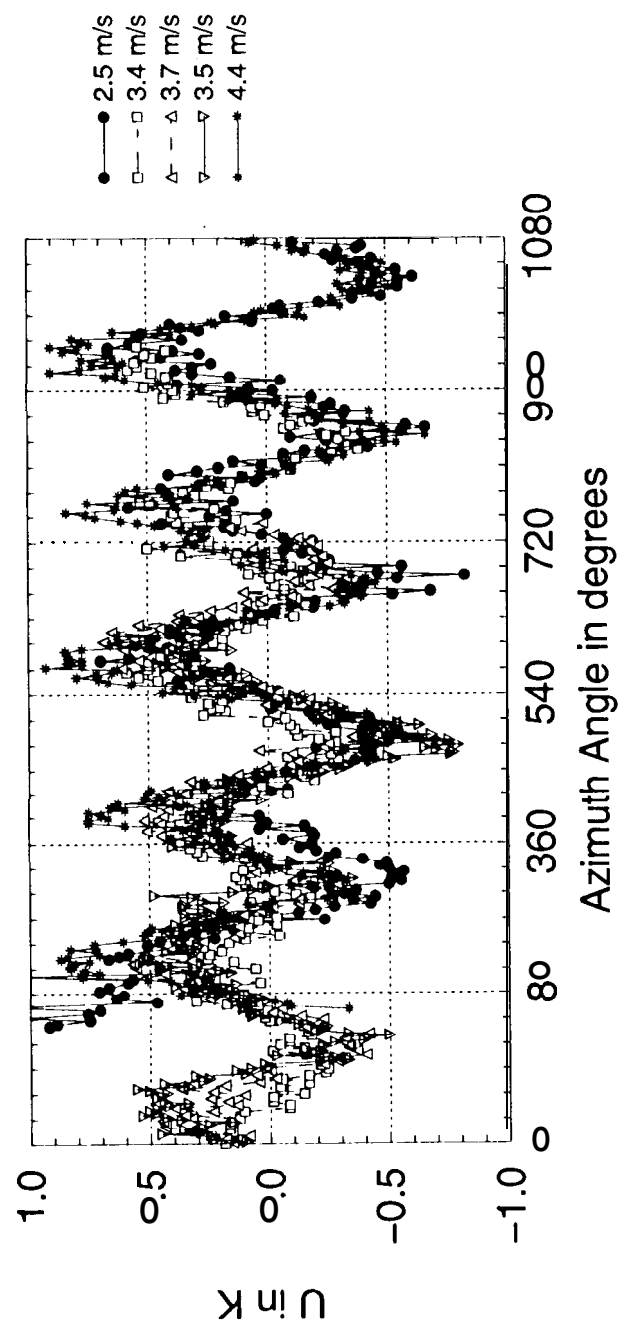


Fig 14